Materials Today Chemistry 33 (2023) 101681

Contents lists available at ScienceDirect

Materials Today Chemistry

journal homepage: www.journals.elsevier.com/materials-today-chemistry/

Facile growth of perovskite nanoparticles confined on dimension-controlled Si nanorod arrays for various promising photophysical applications

Ramesh Ghosh [a,*,1], Joydip Ghosh [b,1,2], P.K. Giri [b], Puspendu Guha [c,d], Gyu-Chul Yi [c,d]

[a] James Watt School of Engineering, University of Glasgow, Glasgow, G12 8QQ, United Kingdom
[b] Department of Physics, Indian Institute of Technology Guwahati, Guwahati, 781039, India
[c] Department of Physics and Astronomy & Institute of Applied Physics, Seoul National University, Seoul, 08826, Republic of Korea
[d] Research Institute of Advanced Materials (RIAM), Seoul National University, Seoul, 08826, Republic of Korea

ARTICLE INFO

Keywords:
Perovskite nanoparticles
Mesoporous Si nanorods
Photoluminescence enhancement
Cathodoluminescence

ABSTRACT

In this study, a facile growth of hybrid perovskite nanoparticles (NPs) has been demonstrated on mesoporous, high-aspect ratio, morphology-controlled Si nanorod (NR) arrays. A generic method of directly confining perovskite nanocrystallites (average size <7 nm) on a mesoporous substrate without the use of colloidal stabilization was introduced. The perovskite NPs coated on dimension-and position-controlled Si NR arrays were systematically investigated by their various photophysical properties such as optical reflectance, cathodoluminescence (CL), and photoluminescence (PL) behaviors at both room temperature and low temperature. The dimension and position of the Si NR arrays were controlled by e-beam lithography followed by selective metal-assisted chemical etching (MACE). Organic-inorganic perovskite NPs were synthesized on the surface of Si NR array by spin coating of perovskite precursor solution and followed by annealing. The porous and rough sites on the surface of the NR arrays acted as nucleation centers for the formation of perovskite NPs. Due to the excitonic recombination of $CH_3NH_3PbBr_3$, the NPs confined on the various NR templates exhibited strong PL emission in the 505–510 nm region. Furthermore, due to greater radiative recombination and lesser carrier trapping in the NPs, the PL and CL emission intensities of the perovskite NPs localized on the surface of the NR array were dramatically increased (PL enhancement factor ~ 7.7, when NR aspect ratio ~ 17.2) as compared to the bulk perovskite microcrystals. The low-temperature PL study revealed higher exciton binding energy of the NPs as compared to the bulk microcrystalline film. A systematic investigation revealed that the optical absorption, as well as the emission color of the perovskite NPs, can be tuned by the aspect ratio of the Si NR arrays. The results of our studies indicate the application of bandgap engineering of perovskite nanocrystals through confinement in a mesoporous, well-organized, regularly-ordered template as a powerful tool for tuning the emission wavelength in next-generation photonic sources. Furthermore, the important findings on the periodic array of photoactive nanoscale materials introduced in this manuscript may open up huge opportunities in numerous cutting-edge applications such as light emitting diode arrays, photodetector arrays, individually addressable devices, display devices with controlled pixel size and pixel density, etc.

1. Introduction

Organic-inorganic halide perovskite nanomaterials, especially quantum-size perovskite nanoparticles (NPs), have attracted researchers' attention worldwide for over a decade because it is considered to be a game changer in optoelectronics [1–8]. Enormous advancement has been made in halide perovskite for understanding the fundamental photophysical and photochemical properties in nanoscale dimension to overcome the challenges in photovoltaics, light emitting diodes (LEDs), energy storage, photodetection, photocatalysis, and display applications [1–10]. Interestingly, tunable optical properties of halide perovskite NPs turned out to be a new class of nanomaterial for LED and display applications as its color can be tuned across the entire visible light spectrum by just tuning NP size, shape, and halide

* Corresponding author.
E-mail address: Ramesh.Ghosh@glasgow.ac.uk (R. Ghosh).
[1] Authors equally contributed in this work.
[2] Present address: Department of Physics, University of Surrey, Guildford, Surrey GU2 7XH, U.K.

https://doi.org/10.1016/j.mtchem.2023.101681
Received 11 May 2023; Received in revised form 27 June 2023; Accepted 2 August 2023
Available online 8 August 2023

composition [11–15]. The development of perovskite NP synthesizing techniques that enable better control over shape and size was spurred on by this, which sparked an upsurge in research in this field. Out of different synthesizing methods, the template-assisted method has emerged as a powerful technique for the synthesis of encapsulation-free perovskite NPs with controlled dimensions and shape.

Mostly mesoporous matrixes, such as mesoporous silica, alumina (Al_2O_3), porous titanium dioxide (TiO_2), zeolite-Y composite, and metal−organic frame-works, Si nanowires (NWs), etc. have been used as an efficient template to synthesize dimension-controlled perovskite NPs [16–31]. Porous Si is a well-known versatile template and an active host material over the years for hosting a variety of nanocrystals including metallic nanoparticles, semiconductors as well as organic polymers [32–35]. Instead of porous Si film, high-aspect-ratio mesoporous Si nanostructure based-templates have been found more advantageous over the other templates in terms of optoelectronic device applications. Due to their superior physical and chemical qualities, eco-friendliness, and high device compatibility, 1D Si nanorods (NRs)/NWs, at present, are the most commonly utilized material in nanotechnology applications [32,36,37]. In integration with the guest nanomaterial, the host mesoporous Si nanostructures trigger new functionalities superior for synergistic application. The ability to manipulate the locations and morphologies of active nanostructures is a well-known necessity for using nanostructures as foundational components for developing various kinds of photonic and optoelectronic nanodevices. Here are a few of the main benefits of uniform array of nanostructures. (a) A better knowledge of the material characteristics and improved device performance are provided by regular arrays of uniform-sized nanomaterials [38]. (b) In the case of a display device or image sensor, a controlled pixel array can be built depending on the size and spacing of the nanostructure arrays [39]. (c) The manufacturing of complicated devices and their close-packed integration for practical applications benefit geometrically from site-specific & aligned 1D nanostructures [39]. For instance, the vertically well-aligned 1D nanostructures allow for the local metalization of the nanostructures' selected regions along their own axis. As a result, vertical 1D nanostructure-based heterojunction arrays are suitable to build vertical 3-terminal devices [40,41]. (d) The parasitic effect and non-unity ideal factor brought on by the formation of undesired cross-connections between closely packed devices can be significantly reduced by the well-organized 1D nanostructure arrays [42]. These motivate to introduce dimension-as well as position-controlled mesoporous Si NR arrays as an efficient and active template for the growth of perovskite NPs and investigate the photophysical properties of the heterostructures for their potential nanotechnology applications.

In this study, we have investigated the synthesis of $CH_3NH_3PbBr_3$ NPs on a mesoporous, high-aspect ratio, morphology-controlled Si NRs arrays and investigated its photophysical properties by means of optical reflectance, cathodoluminescence (CL), and photoluminescence (PL) behaviors at both room temperature and low temperature. The dimension and position of the Si NRs are controlled by e-beam lithography followed by selective metal-assisted chemical etching (MACE) [36,43]. Perovskite NPs were grown on the surface of Si NR array by spin coating of perovskite precursor solution and followed by annealing. The porous sites on the surface of the NRs array act as nucleation centers of perovskite NPs. The PL and CL emission intensities of the perovskite NPs confined on the surface of the NR array were significantly enhanced as compared to the bulk perovskite microcrystals due to high radiative recombination and lower carrier trapping. The low-temperature PL study reveals higher exciton binding energy of the NPs as compared to the bulk film. A systematic investigation revealed that the optical absorption, as well as the emission color of the perovskite NPs, can be tuned by the aspect ratio of the Si NR arrays. The important findings in this manuscript may open up huge opportunities for the perovskite NP-embedded Si NR arrays to be utilized in different cutting-edge applications.

2. Experimental details

2.1. Materials

Methylammonium bromide (CH_3NH_3Br, Sigma Aldrich), methylammonium iodide (CH_3NH_3I, Sigma Aldrich), lead(II) bromide ($PbBr_2$, Sigma Aldrich), lead(II) iodide (PbI_2, Sigma Aldrich), N,N-dimethyl formamide (DMF, >99%, Sigma Aldrich), H_2O_2 (50%, Sigma Aldrich), HF (48%, Sigma Aldrich), etc. were purchased.

2.2. Fabrication of dimension and position-controlled Si NR arrays

The mesoporous Si NR arrays were fabricated by the well-known metal-assisted chemical etching (MACE) method using Si wafer at 25 °C [30,43,44]. Si (100) wafers with resistivity 0.001 Ω-cm and thickness 500 μm were first cleaned by the typical Radio Corporation of America (RCA) cleaning process [44]. Next, a uniform pattern of negative e-beam resist MaN-2405 was created by e-beam lithography followed by a deposition of a thin Au layer (15 nm) by evaporation process. A uniform hole array pattern of Au was made by immersing the wafers in acetone. The Au-patterned Si wafers were then dipped into a solution containing HF and H_2O_2 with different concentrations. Dimension and position-controlled Si NR arrays were formed with different lengths depending upon the etching duration. 5, 10, 15, 20, and 30 min etched samples are 8:1 (M) HF:H_2O_2 were termed as NR1, NR2, NR3, NR4 and NR5, respectively. Finally, the residual Au particles in the samples were cleaned with KI:I_2 solution. The Si NR samples were ringed with DI water several times and dried in N_2 gas flow.

2.3. Synthesis of $CH_3NH_3PbBr_3$ NPs

0.5 M $CH_3NH_3PbBr_3$ precursor solution was prepared in N,N-dimethyl formamide (DMF) by mixing 0.5 M CH_3NH_3Br and 0.5 M $PbBr_2$. The prepared solutions were deposited on the Si NR and Si wafer templates by spin coating method at 2000 rpm for 40 s. After the spin coating, the samples were baked on a hot plate at 85 °C for 15 min, which results in the formation of crystalline $CH_3NH_3PbBr_3$ on the Si surface. The sample details and the respective sample codes are summarized in Table 1.

2.4. Characterization techniques

A field emission scanning electron microscope (FESEM, TESCAN) equipped with an energy dispersive x-ray (EDX) spectrometer was used to characterize the morphology and elemental compositions of different samples. The decorations of perovskite NPs on the NR surface and the crystal lattice fringes were studied by a field-emission transmission electron microscope (FETEM) with 200 kV acceleration voltage (analytical TEM, JEM-2100F, JEOL Ltd. equipped with energy-dispersive x-ray spectroscopy (EDS)). To investigate the structural characterization and the elemental analyses by FETEM, bare Si NRs and perovskite NP-coated NRs were scratched and dispersed in isopropanol, then drop-casted on the lacey carbon-coated Cu TEM grid. X-ray

Table 1
Sample description for $CH_3NH_3PbBr_3$.

Sample Code	Si NR Etching Condition	Si NR Etching Time	Perovskite Coating		
			Precursor	Precursor Ratio	Growth Condition
BulkPe			0.5 M CH_3NH_3Br in 1 ml DMF & 0.5 M $PBBr_2$ in 1 ml DMF	1:1	0.5 M $CH_3NH_3PbBr_3$, 2000 rpm, 40 s, 85 °C, 15 min
NR1Pe	HF:H_2O_2 = 8:1 (M), 25 °C	5 min			
NR2Pe		10 min			
NR3Pe		15 min			
NR4Pe		20 min			
NR5Pe		30 min			

diffractometer (XRD) (Rigaku RINT 2500 TRAX−III, Cu Kα radiation) was used for the determination of the phase and structure of $CH_3NH_3PbBr_3$ NPs. UV–vis diffuse reflectance spectra (DRS) were recorded using a commercial spectrophotometer equipped with an integrating sphere (PerkinElmer, Lamda 950). Room temperature cathodoluminescence spectra were recorded using Gatan Mono CL4 attached to the FESEM. A commercial fluorimeter (Horiba Jobin Yvon, Fluoromax-4) was used to record the room temperature steady-state PL spectra of different samples using a 405 nm diode laser (CNI Laser) excitation along with a band pass filter. Low-temperature PL measurements were performed by using He-cryostat equipped with CCD detector. Time-resolved PL (TRPL) measurements of the samples were carried out using a 405 nm pulsed laser excitation, with an instrument time response of <50 ps (LifeSpecII, Edinburgh Instruments). All the fabrication and characterization were performed in an open-air atmosphere without any humidity control.

3. Results and discussion

3.1. Morphology and structure

Prior to the perovskite coating, dimension and position-controlled Si NR arrays were prepared by an Au-assisted chemical etching process. 15 nm thick hole array pattern was created by e-beam lithography. Fig. 1(a) shows the FESEM image of the 500 nm hole array pattern of Au on Si wafer. Fig. 1(b) shows the FESEM image of the corresponding etched sample indicating the top-view of Si NR arrays having a diameter of 500 nm. Fig. 1(c–g) depicts the 30° tilt-view FESEM images of the Si NR arrays in samples NR1, NR2, NR3, NR4, and NR5, respectively, while Fig. 1(h) shows the length of the Si NRs as a function of etching duration. Note that the MACE-grown Si NRs are vertically aligned and merged together towards the top side for a prolonged together, which also depends on the NR spacing. The FESEM images of $CH_3NH_3PbBr_3$-coated Si wafer (BulkPe) and Si NR (NR2Pe) are shown in Fig. 2(a) and (b), respectively. It is clear that the cubic $CH_3NH_3PbBr_3$ microcrystals are formed in the case of BulkPe, while $CH_3NH_3PbBr_3$ NPs are not visible in sample NR2Pe due to its ultra-small size. The formation of the $CH_3NH_3PbBr_3$ NPs on the surface of the Si NRs is confirmed by the EDS analysis, as shown in Fig. 2(c). An elemental mapping of NR2Pe is shown in Fig. S1 (Supporting Information) for further support.

To confirm the phase and crystalline quality of $CH_3NH_3PbBr_3$ on Si NR and Si wafer, X-ray diffraction (XRD) study was performed. The sharp diffraction peaks in Fig. 2(d) confirm the highly crystalline nature of perovskite NPs and film. The XRD peaks at 14.97°, 21.27°, 30.21°, 33.93°, 37.11°, 44.58°, and 45.9° of the samples correspond to (100), (110), (200), (210), (211), (220) and (300) planes of $CH_3NH_3PbBr_3$, respectively while the peak at 69.09° is associated to the (400) planes of Si.

Fig. 3(a) shows the bright-field (BF) low-magnification TEM image of a single mesoporous Si NR decorated with $CH_3NH_3PbBr_3$ NPs (sample NR2Pe). The high-resolution TEM image (Fig. 3(b)) further indicates the magnified view of the surface morphology of the mesoporous Si NR decorated with $CH_3NH_3PbBr_3$ NPs. Note that the Si NR surface is highly porous and rough in nature [36,37,44–46]. The size of the porous sites as well as the formed nano-islands in between them, typically ranged from 2 to 10 nm [36]. These porous sites act as nucleation sites for the formation of the perovskite NPs. Interestingly, the shape and size of the perovskite NPs are restricted to the dimension of the porous sites, which could be estimated from the mesoporous dimension of the Si NR. Interestingly the size of the NPs is comparable to the excitonic Bohr diameter of $CH_3NH_3PbBr_3$ [47,48]. Thus, quantum size perovskite NPs are formed on the surface of Si NR, which results in strong room temperature CL and PL emission [30,31]. Note that the formation mechanism of perovskite NPs in mesoporous substrate is already reported in earlier reports [30,31]. In this method perovskite nanocrystallites (average size <7 nm) are directly confined on a mesoporous substrate which is organized in the from of a regular array. The HRTEM lattice fringe image in Fig. 3(b) confirms the high crystalline quality of the $CH_3NH_3PbBr_3$ structure [11]. High-angle annular dark-field (HAADF) scanning transmission electron microscopy (STEM) images of a mesoporous Si NR decorated with $CH_3NH_3PbBr_3$ NPs in sample NR2Pe are shown in Figs. S2(a–c) (Supporting Information) along with the inverse fast Fourier transform (IFFT) images of Fig. 3(b) at two different positions in Figs. S2(d–e) (Supporting Information). The bright diffraction spot in the SAED pattern (Fig. 3(c)) corresponds to the (200) plane of cubic $CH_3NH_3PbBr_3$ structure [11,31]. The elemental distribution of the perovskite NPs decorated NR in sample NR2Pe was further characterized by elemental mappings in a STEM mode. Fig. 3(d–h) shows the

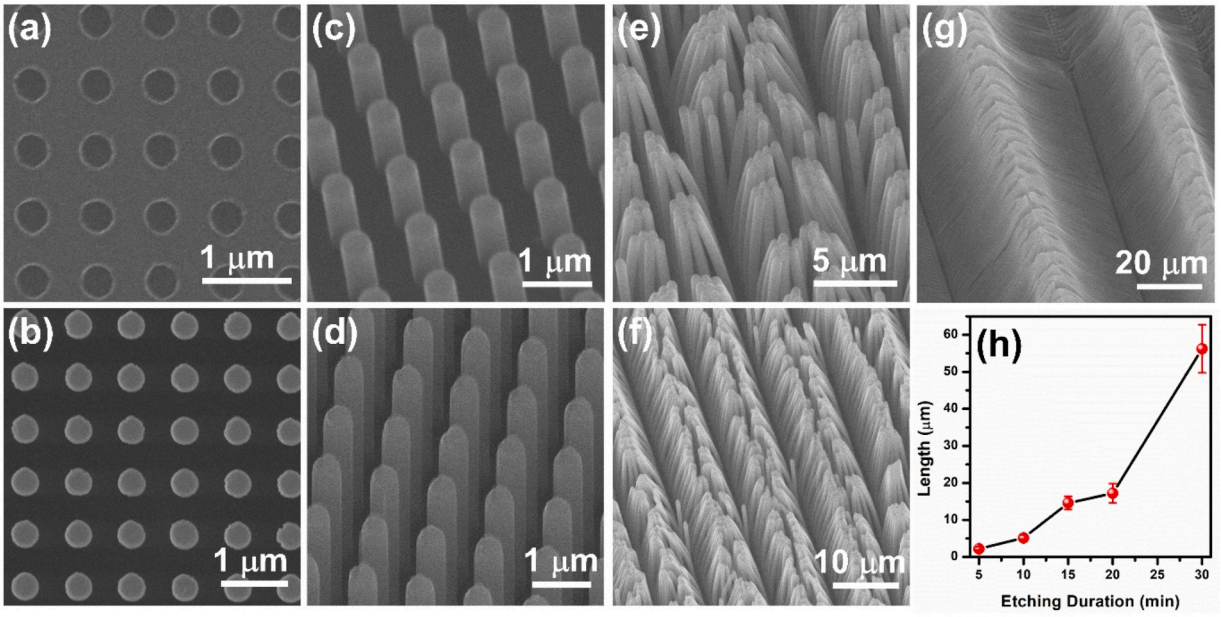

Fig. 1. (a) The SEM image of the patterned Au film on Si wafer. (b) Top view SEM image of the Si NR arrays etched for 10 min (NR2). (c–g) 30° tilt-view SEM images of the Si NR arrays in sample NR1, NR2, NR3, NR4 and NR5, respectively. (h) The length of the Si NRs as a function of etching duration.

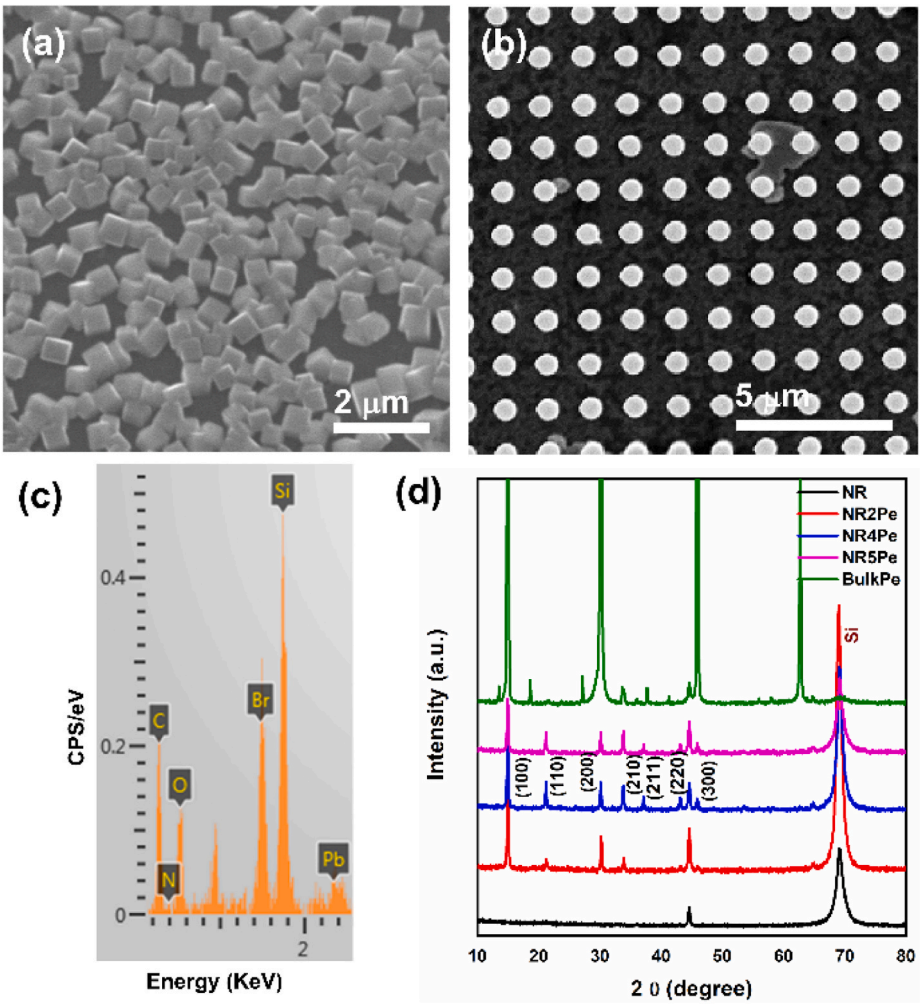

Fig. 2. (a,b) The SEM image of the sample BulkPe and NR2Pe, respectively. (c) The EDS spectrum for the sample NR2Pe. (d) The comparison of the XRD spectra collected from different samples. The spectra are vertically shifted for enabling the comparison.

elemental color mapping of $CH_3NH_3PbBr_3$ NP-coated Si NR corresponds to Si, Pb, Br, C, and N elements, respectively, while Fig. 3(i) shows the corresponding STEM-HAADF image. Fig. 3(j) shows the corresponding EDS spectrum with an atomic percentage in a tabulated form. However, a regularly-ordered and organized array of photoactive nanoscale materials are introduced which is composed of perovskite NPs and mesoporous Si NRs.

3.2. Diffuse reflectance spectroscopy

We have observed a significant change in reflectance acquired from $CH_3NH_3PbBr_3$ NPs on Si NRs for different samples. In order to investigate the nature of the absorption band-edge of the perovskite NPs and bulk counterpart, the Kubelka−Munk (KM) function is calculated by using the relation,

$$KM(R) = \frac{(1-R)^2}{2R} = \frac{K}{S} \quad (1)$$

where R is the diffuse reflectance of the samples, K and S are the absorption and scattering coefficients, respectively. Fig. 4 shows the comparison of the KM function of BulkPe and different perovskite NPs coated on NRs in a stacked way. Similar measurements are also done for the $CH_3NH_3PbI_3$ decorated Si NRs and the corresponding KM function data are shown in Fig. S3(a) (Supporting Information), respectively. Interestingly, the absorbance edge is systematically blue-shifted for the perovskite NPs confined on the surface of the NR array as compared to the perovskite film, which may be due to the quantum confinement effect and increase in bandgap on the perovskite NPs [19,49]. The shift in absorption edge acquired from $CH_3NH_3PbBr_3$ and $CH_3NH_3PbI_3$ are compared in Fig. S3(b) (Supporting Information). Note that the blue shift of the absorption edge increases with increasing the etching duration of Si NRs. It is mentioned that the perovskite NPs are formed on the mesoporous sites on the Si NRs. The prolonged etching results in an increase in the density of porous sites as well as a reduction in pore size because of the splitting of Si nano-islands. As a result, the average sizes of perovskite NPs are decreased while their density is increased for Si NR substrate etched for a longer time. As an outcome, the adjustable absorption from the perovskite NPs suggests the utilization of bandgap engineering of perovskite NPs without altering the halide atoms by confinement in a mesoporous, well-organized, regularly-ordered template, which is much more advantageous for photovoltaic application.

3.3. Photoluminescence and cathodoluminescence

PL measurement was performed to evaluate the light emission properties of perovskite NPs confined on the surface of the Si NR array. Fig. 5(a) presents the comparison of PL spectra of $CH_3NH_3PbBr_3$ NPs confined on the different NR templates. The inset of Fig. 5(a) shows the PL spectra of bulk perovskite film on a Si substrate. All the $CH_3NH_3PbBr_3$ NPs confined on the different NR templates show strong PL emission in the range of 505–510 nm due to the excitonic recombination of

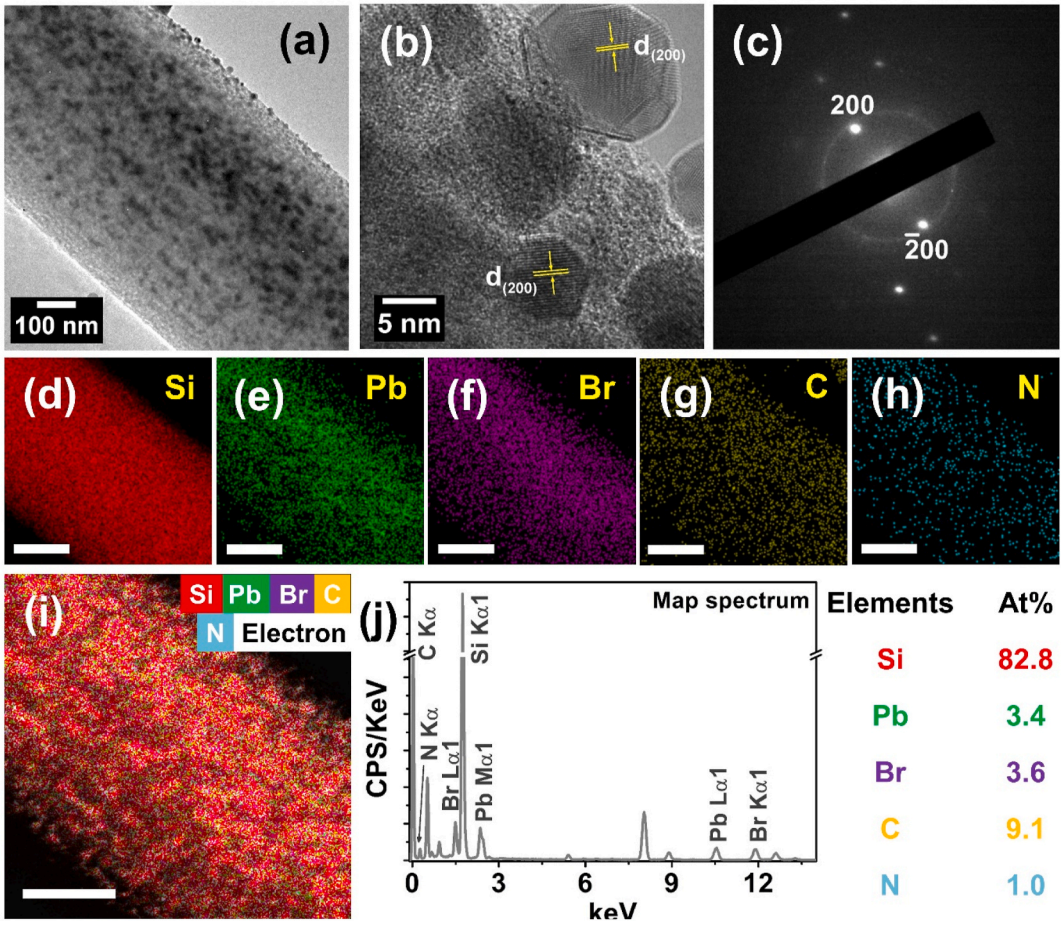

Fig. 3. (a) Bright-field (BF) low magnification TEM image of a single mesoporous Si NR decorated with $CH_3NH_3PbBr_3$ NPs (Sample NR2Pe). (b) HRTEM lattice fringe image of quantum size $CH_3NH_3PbBr_3$ NPs. (c) SAED pattern on the surface of $CH_3NH_3PbBr_3$ NP-coated Si NR. Elemental color mapping of $CH_3NH_3PbBr_3$ NP-coated Si NR: (d) Si, (e) Pb, (f) Br, (g) C, and (h) N elements and (i) the corresponding STEM-HAADF with composite elemental color mapping of $CH_3NH_3PbBr_3$ NP-coated Si NR (all the scale bars correspond to ~200 nm); (j) corresponding EDS spectrum with atomic % in a tabulated form.

$CH_3NH_3PbBr_3$ perovskite. The PL peak intensities of the NPs samples were significantly enhanced as compared to that of bulk perovskite, which is attributed to the quantum confinement and high radiative recombination in NPs. The high surface area of NPs confined on the NR arrays may also contribute to the PL enhancement in the NPs samples. PL peak intensities as well as the integrated peak intensities were enhanced by increasing the NR length as shown in Fig. S4 (Supporting Information). However, the peak enhancement factors for the Per NPs on 5, 10, 15, 20, and 30 min etched Si NRs were found to be 4.8, 5.0, 6.0, 7.7, and 8.7, respectively. The enhancement in the PL intensity with the increase in NR lengths was primarily attributed to the higher volume of NPs exposed to the incident laser excitation. Furthermore, earlier reports suggest that the porosity of Si NRs increases with the increase of NR etching duration because of the lateral etching [36,37,44,50,51]. Hence, during the formation of perovskite NPs the corresponding NP density was increased with the length of Si NRs and this played a crucial role for the enhancement of PL peak intensity. It can be noted that the increasing trend of perovskite PL intensity with Si NR etching duration was slower than that of for the Si NR length (Fig. 5(b)). Thus, the PL peak intensity is expected not to maintain a monotonic increasing trend. This is because of the unaltered NP density after a certain period of Si NR etching duration. Existing literature suggests that the impurities, dopants, etc. present in the Si wafer that is etched to create Si NRs are responsible for the lateral etching of Si NRs [36,37,44,46,50]. Since the impurities, dopants, etc. are limited, the lateral etching is usually stopped after a certain time and porosity is unaltered even further etching of Si NRs vertically. On the other hand, the top ends of the ultra-long Si NRs try to bend and merge together (Fig. 1(e–g)), which can also reduce the effective surface area and hence the PL peak intensity. The variation of the PL peak intensity and PL peak shift ($\Delta\omega$) of the NPs confined on the different NR array templates versus NR etching time is shown in Fig. 5(b). The right Y axis of Fig. 5(b) shows the comparison of the length of the NRs calculated from the SEM images with MACE etching time. The PL peak positions of the NPs were blue-shifted as compared to that of the bulk film due to an increase in band gap and quantum confinement effect. Note that we observed a bule shift of K-M function edge in the NPs sample. Fig. 5(c) shows the comparison of PL peak positions and the center of the absorption edge of the $CH_3NH_3PbBr_3$ NPs samples with NR etching time. Interestingly the blue shift was increased in the NR sample with a higher etching time. With the increase in MACE times, high-density smaller size pores grow on the surface of the NR array which may result in smaller size perovskite NPs. Though the PL shifts for both the two different groups of $CH_3NH_3PbI_3$ and $CH_3NH_3PbBr_3$ samples showed a similar trend (Fig. S6(a) ((supporting information))), the bromine-based samples exhibited a slightly higher blue shift as compared to the iodine-based samples with the increase in NR lengths. This may be attributed to the different shapes and sizes of the NPs of bromine and iodine-based samples. The different reduced mass of exciton in the two different perovskites may also result in the different peak shifts. In case of PL intensity enhancement, the iodine-based samples exhibited a higher enhancement factor for a fixed Si NR length as compared to same for the bromine-based samples (Fig. S6(a) ((supporting information))). This is possibly because of the reabsorption process in case of the $CH_3NH_3PbI_3$ samples [30,52]. Note

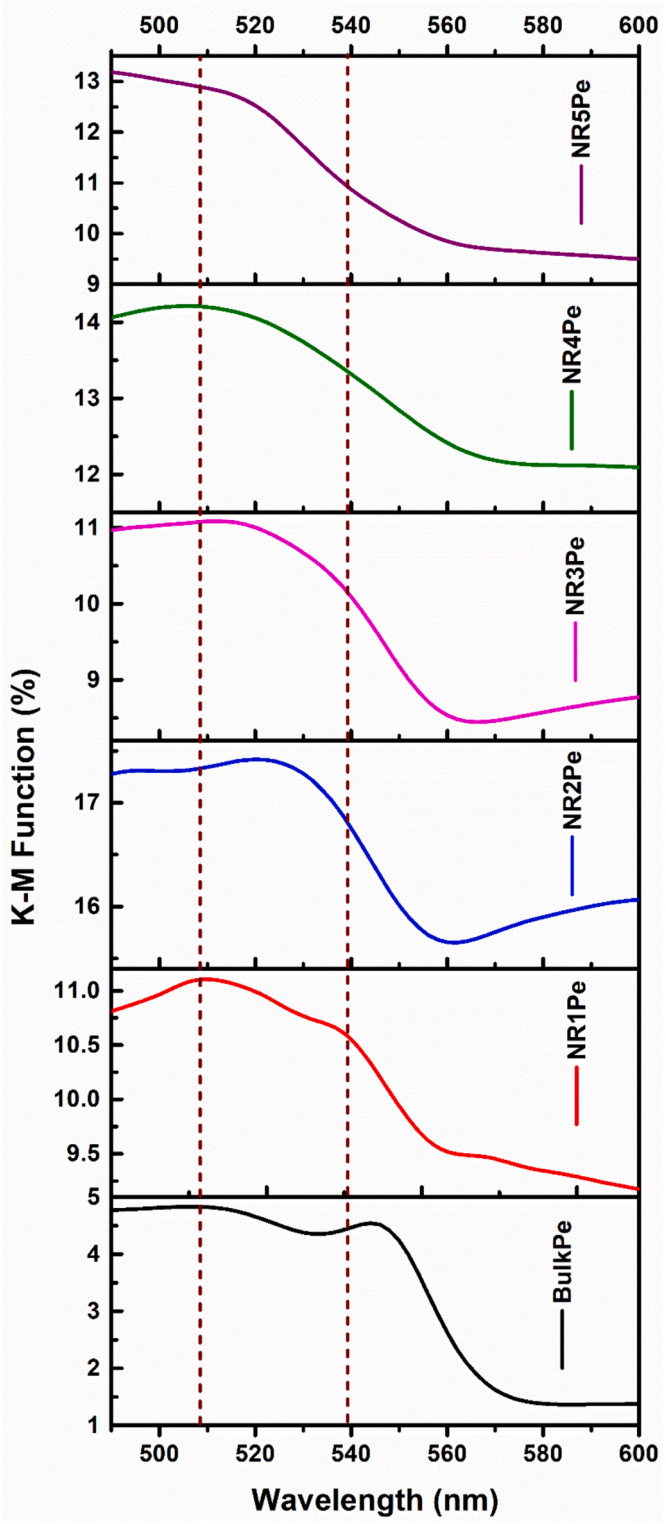

Fig. 4. Comparison of the Kubelka–Munk (K–M) function calculated from the reflectance data acquired from the sample BulkPe, NR1Pe, NR2Pe, NR3Pe, NR4Pe and NR5Pe, respectively.

that Si NRs showed a broad PL covering almost the entire visible range with a peak position at 690–715 nm (Fig. S7((supporting information)). The $CH_3NH_3PbI_3$ NP samples exhibited absorbances those had a strong overlap with the Si NR PL, which was almost negligible/absent for the bromine-based perovskite NPs. Thus, the iodine-based perovskite NPs can reabsorb the emitted photons by the Si NRs, and this photon recycling may result in high-intensity PL from the $CH_3NH_3PbI_3$ NP samples.

PL measurement was also performed on $CH_3NH_3PbI_3$ NPs confined on the surface of the Si NR array, as shown in Figs. S5(a–b) (Supporting Information). In a similar fashion, the PL peak intensities of the NPs samples were significantly enhanced and corresponding peak positions were blue-shifted as compared to that of bulk perovskite (as shown in Fig. S5(c) (Supporting Information)). A comparison of PL peak shift and PL peak enhancement factor for $CH_3NH_3PbBr_3$ and $CH_3NH_3PbI_3$ NPs with the increase in length of the NR array are compared in Figs. S6(a–b) (Supporting Information). The $CH_3NH_3PbBr_3$ NP samples showed larger peak shifts as compared to $CH_3NH_3PbI_3$ NP samples, whereas the enhancement factor was dramatically increased for $CH_3NH_3PbI_3$ NPs with the Si NR length. However, earlier research suggest the stability of PL is significantly increased by confining perovskite nanocrystals in mesoporous templates [20,31]. In this class of materials, the colour tunability or bandgap engineering is typically accomplished through modifying the chemical composition, nanostructuring, and quantum confinement [53]. Thus, the strong, tunable and stable PL emission from the perovskite NPs in the present studies indicate the application of bandgap engineering of perovskite NPs through nanostructuring and confinement in a mesoporous, well-organized, regularly-ordered template, which can be utilized as a effective method for the manufacturing of next-generation photonic sources.

We further study the cathodoluminescence behavior of the samples. Fig. 5(d) depicts the comparison of CL spectra of samples BulkPe, NR2Pe and NR4Pe under the excitation of the electron beam accelerated with 15 kV. Perovskite NPs confined in Si NR template exhibit stronger CL emission as compared to the bulk counterpart due to higher radiative recombination and low carrier trapping in the perovskite NPs. The CL peak also blue-shifted for the NPs samples grown on NR template, which is consistent with the PL study. The strong and tunable light emission from the perovskite NPs confined on dimension- and position-controlled Si NRs opens up the future application of the material system for various photonic and optoelectronic devices which include addressable LED arrays, photodetector arrays, display devices with controlled pixel size and pixel density, etc.

3.4. *Low-temperature photoluminescence*

We further studied the temperature-dependent PL of $CH_3NH_3PbBr_3$ NPs confined on the Si NR template to investigate the origin of high PL emission of the NPs. Fig. 6(a) and (b) depict the PL spectra of sample BulkPe and NR2Pe, respectively, in the temperature range 11 K–300 K. With the increase in temperature, the PL peak intensities of the samples were decreased due to the high radiative recombination at low-temperature. The PL peak of the samples was red-shifted with the decrease in temperatures, which is attributed to the lattice thermal expansion with a positive temperature coefficient (as shown in Fig. 6 (c)). The PL spectra of the samples contain multiple peaks at low temperature regime, which may be due to the coexistence of multiple phases of perovskites and emission from free and bound excitons [54–56]. For example, $CH_3NH_3PbBr_3$ perovskite exhibits three different phases, orthorhombic (<145 K), tetragonal (145−237 K), and cubic (>237 K), which emits at different wavelengths [55]. Shinde et al. claimed at low temperatures, the higher-energy component is associated with the free excitonic recombination, while the low-energy peak originates from the bound excitonic recombination [54].To estimate the exciton binding energy (E_B) of $CH_3NH_3PbBr_3$ NPs embedded in NR template and bulk perovskite film, we have fitted the integrated PL peak intensity versus the inverse of temperature (1/T) (Fig. 6(d) and (e)) using an Arrhenius-like equation as followed by:

$$I(T) = \frac{I_0}{1 + A\exp(-E_b/k_BT)} \quad (2)$$

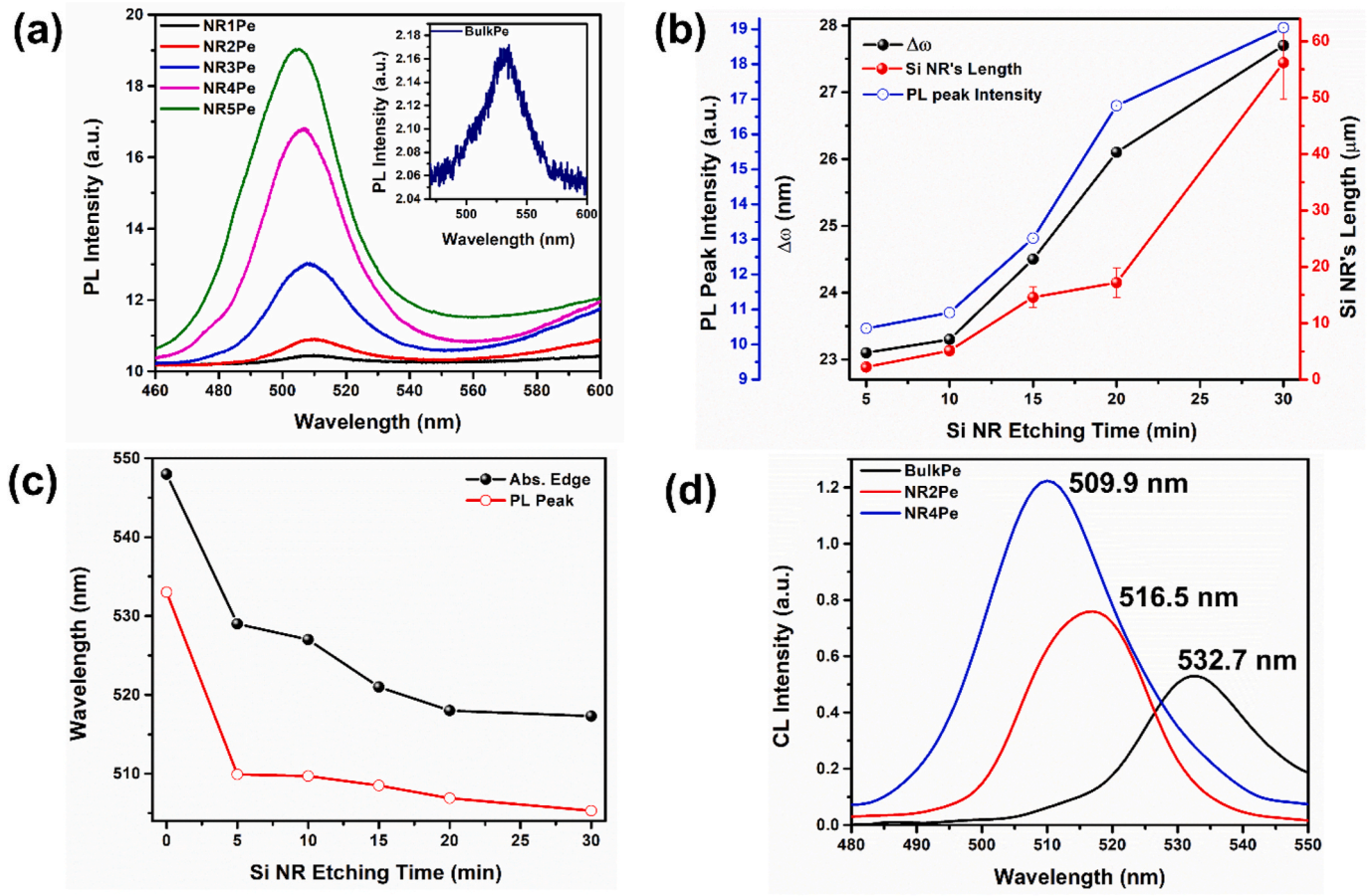

Fig. 5. (a) Comparison of the RT PL spectra acquired from the sample NR1Pe, NR2Pe, NR3Pe, NR4Pe and NR5Pe respectively. Inset shows the corresponding spectrum for BulkPe. (b) The variation of PL peak shift (Δω) and PL peak intensity as a function of Si NR etching time. The length of the Si NR arrays is also estimated. (c) Comparison of the PL peak shift (Δω) and shift is absorption edge of the different perovskite QD samples. (d) Comparison of the RT CL spectra acquired from the sample NR2Pe, NR4Pe and BulkPe, respectively.

where I_0 is the integrated PL peak intensity at very low temperature, and k_B is the Boltzmann constant. The exciton binding energy was obtained to be 55.5 meV for sample NR2Pe while for bulk perovskite film, it was calculated to be 37.5 meV. Thus the E_B was significantly increased for the NPs sample as compared to the bulk film due to the quantum confinement effect. When nanostructure sizes become smaller/comparable to the bulk exciton Bohr radius, excitonic effects are significantly enhanced with a strong quantum confinement effect [57]. The electron-hole Coulombic interactions that give rise to these excitonic effects significantly strengthen the oscillation between the electron and the hole in the quantum size NPs [58]. Thus the quantum confinement results in larger exciton binding energies and normalized exciton oscillator strengths in the NPs confined on the NR array template as compared to the bulk perovskite film [59].Thus, the high exciton binding energy of $CH_3NH_3PbBr_3$ NPs embedded in NR surface is consistent with the high PL emission intensity at room temperature.

3.5. Time-resolved photoluminescence

In order to investigate photo carrier recombination kinetics of the $CH_3NH_3PbBr_3$ NPs and the bulk perovskite film, time-resolved photoluminescence (TRPL) measurements were performed. Fig. 7 presents a comparison of the TRPL decay time profiles of different NPs samples and bulk film. The TRPL decay profiles were fitted using a tri-exponential function given by:

$$A(t) = A_1 \exp\left(\frac{-t}{\tau_1}\right) + A_2 \exp\left(\frac{-t}{\tau_2}\right) + A_3 \exp\left(\frac{-t}{\tau_3}\right) \quad (3)$$

where A_1, A_2, and A_3 are the amplitudes with decay times of τ_1, τ_2, and τ_3, respectively. The average decay constant (τ_{ave}) was calculated by using the equation.

$$\tau_{ave} = \frac{\sum_{i=1}^{i=3} A_i \tau_i^2}{\sum_{i=1}^{i=3} A_i \tau_i} \quad (4)$$

Different decay time constants and their weightage are tabulated in Table S2 (Supporting Information). The average decay constants were obtained to be 4.9, 4.7,4.8, 5.0, 6.2 and 6.7 ns for samples BulkPe, NR1Pe, NR2Pe, NR3Pe, NR4Pe and NR5Pe, respectively. Thus the decay time constants were increased in the NPs as compared to the bulk counterpart which may be attributed to the high radiative recombination of carriers in the NPs confined on the NR templates. Thus the high radiative carrier recombination results in high PL and CL yield of the NPs samples. The tri-exponential decay times are attributed to band-edge excitonic recombination, shallow trap-mediated radiative recombination, and the trap states arising from the surface defects in the perovskite NPs confined on the porous NR array template [60,61]. Fig. S8 (Supporting Information) depicts the TRPL decay profiles of $CH_3NH_3PbI_3$ NPs confined on different NR templates and bulk film while corresponding decay time constants and amplitudes are added in Table S2 (Supporting Information). Interestingly a similar increase in average decay times was observed for $CH_3NH_3PbI_3$ NPs samples.

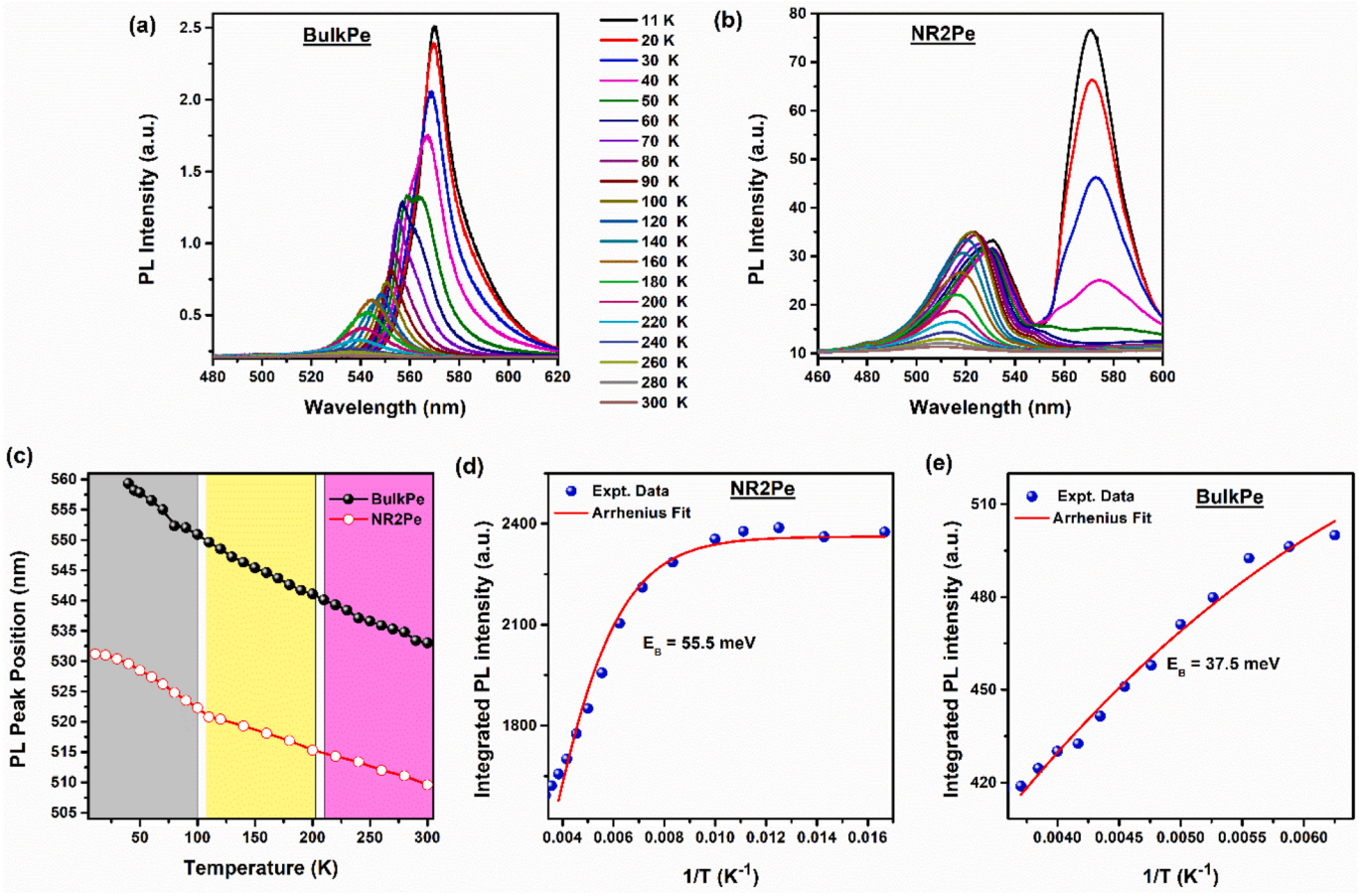

Fig. 6. Temperature-dependent PL spectra of $CH_3NH_3PbBr_3$ on sample (a) BulkPe, (b) NR2Pe. The legends are same (a) and (b). (c) Variation of the PL peak as a function of temperature. (d–e) Arrhenius plot of sample NR2Pe and BulkPe, respectively.

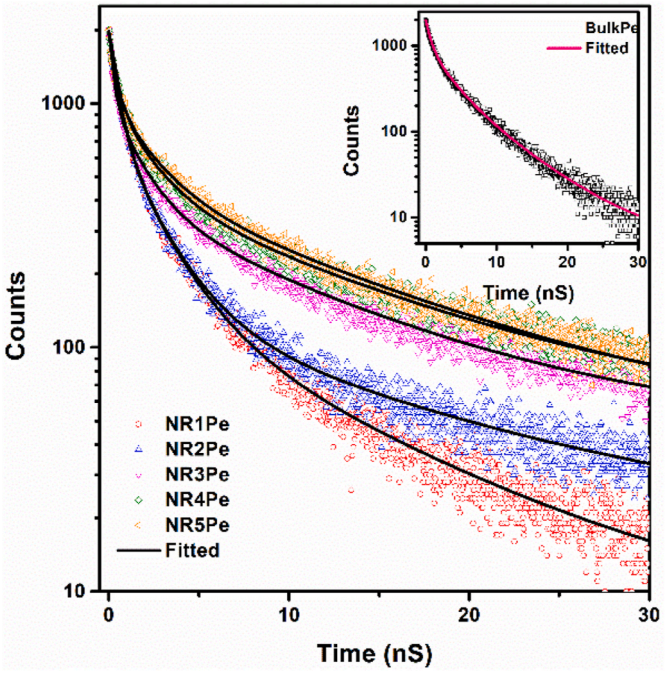

Fig. 7. Comparison of the TRPL spectra for the samples NR1Pe, NR2Pe, NR3Pe, NR4Pe and NR5Pe, respectively. Inset shows the corresponding spectrum for BulkPe.

4. Conclusions

We studied a facile templated growth of hybrid perovskite NPs on a mesoporous, morphology-controlled Si NRs arrays and investigated its photophysical properties by means of optical reflectance, CL, and PL behaviors at room temperature as well as low temperature. The dimension and position of the Si NRs are controlled by e-beam lithography followed by selective MACE process. Organic-inorganic perovskite NPs were synthesized on the surface of Si NR array by spin coating of perovskite precursor solution and followed by annealing. The porous and rough sites on the surface of the NRs array act as nucleation centers of perovskite NPs. Due to greater radiative recombination and lesser carrier trapping in the NPs, the PL and CL emission intensities of the perovskite NPs localized on the surface of the NR array were dramatically increased as compared to the bulk perovskite microcrystals. The low-temperature PL investigation showed that the NPs had a greater exciton binding energy than the bulk microcrystalline film. A thorough analysis indicated that the aspect ratio of the Si NR arrays can be used to adjust the optical absorption as well as the emission color of the perovskite NPs. Thus, the outcomes of our research point to the use of bandgap engineering of perovskite nanocrystals by confinement in a mesoporous, well-organized, regularly-ordered template as an effective method for adjusting the light emission wavelength in next-generation LEDs, display devices and other photonic & optoelectronic devices. Moreover, the utilization of the perovskite NPs integrated with the controlled arrays of Si NRs in a well-organized manner in many cutting-edge applications may be made much easier owing to the important findings in this work.

Author statement

Ramesh Ghosh: Writing – original draft, Writing – review & editing, Conceptualization, Methodology, Investigation, Data curation, Formal analysis. Joydip Ghosh: Investigation, Methodology, Formal analysis, Writing – review & editing. P. K. Giri: Investigation, Formal analysis. Puspendu Guha: Investigation, Formal analysis. Gyu-Chul Yi: Formal analysis, Project administration, Funding acquisition.

Declaration of competing interest

The authors declare that they have no known competing financial interests or personal relationships that could have appeared to influence the work reported in this paper.

Data availability

Data will be made available on request.

Acknowledgment

This work was supported by a National Research Foundation of Korea (NRF) grant funded by the Korean government (MSIT) (NRF-2021R1A5A1032996). We also acknowledge the Brain Korea 21-Plus Program, Seoul National University for providing the financial support to conduct part of this work.

Appendix A. Supplementary data

Supplementary data to this article can be found online at https://doi.org/10.1016/j.mtchem.2023.101681.

References

[1] Y. Liyan, T.B. Alexander, G.L. David, W. Tao, Recent progress and challenges of organometal halide perovskite solar cells, Rep. Prog. Phys. 79 (2016), 026501.
[2] N.-G. Park, M. Grätzel, T. Miyasaka, K. Zhu, K. Emery, Towards stable and commercially available perovskite solar cells, Nat. Energy 1 (2016), 16152.
[3] Y.H. Lee, J. Luo, M.-K. Son, P. Gao, K.T. Cho, J. Seo, S.M. Zakeeruddin, M. Grätzel, M.K. Nazeeruddin, Enhanced charge collection with passivation layers in perovskite solar cells, Adv. Mater. 28 (2016) 3966–3972.
[4] J.-P. Correa-Baena, A. Abate, M. Saliba, W. Tress, T. Jesper Jacobsson, M. Gratzel, A. Hagfeldt, The rapid evolution of highly efficient perovskite solar cells, Energy Environ. Sci. 10 (2017) 710–727.
[5] M. Cao, J. Tian, Z. Cai, L. Peng, L. Yang, D. Wei, Perovskite heterojunction based on CH3NH3PbBr3 single crystal for high-sensitive self-powered photodetector, Appl. Phys. Lett. 109 (2016), 233303.
[6] F. Chen, C. Xu, Q. Xu, Y. Zhu, F. Qin, W. Zhang, Z. Zhu, W. Liu, Z. Shi, Self-assembled growth of ultrastable CH3NH3PbBr3 perovskite milliwires for photodetectors, ACS Appl. Mater. Interfaces 10 (2018) 25763–25769.
[7] M.R. Leyden, L. Meng, Y. Jiang, L.K. Ono, L. Qiu, E.J. Juarez-Perez, C. Qin, C. Adachi, Y. Qi, Methylammonium lead bromide perovskite light-emitting diodes by chemical vapor deposition, J. Phys. Chem. Lett. 8 (2017) 3193–3198.
[8] H. Cho, S.-H. Jeong, M.-H. Park, Y.-H. Kim, C. Wolf, C.-L. Lee, J.H. Heo, A. Sadhanala, N. Myoung, S. Yoo, S.H. Im, R.H. Friend, T.-W. Lee, Overcoming the electroluminescence efficiency limitations of perovskite light-emitting diodes, Science 350 (2015) 1222–1225.
[9] J. Ghosh, P.K. Giri, Recent advances in perovskite/2D materials based hybrid photodetectors, J. Phys.: Materials 4 (2021), 032008.
[10] J. Ghosh, G. Natu, P.K. Giri, Plasmonic hole-transport-layer enabled self-powered hybrid perovskite photodetector using a modified perovskite deposition method in ambient air, Org. Electron. 71 (2019) 175–184.
[11] L.C. Schmidt, A. Pertegás, S. González-Carrero, O. Malinkiewicz, S. Agouram, G. Mínguez Espallargas, H.J. Bolink, R.E. Galian, J. Pérez-Prieto, Nontemplate synthesis of CH3NH3PbBr3 perovskite nanoparticles, J. Am. Chem. Soc. 136 (2014) 850–853.
[12] J.A. Sichert, Y. Tong, N. Mutz, M. Vollmer, S. Fischer, K.Z. Milowska, R. García Cortadella, B. Nickel, C. Cardenas-Daw, J.K. Stolarczyk, A.S. Urban, J. Feldmann, Quantum size effect in organometal halide perovskite nanoplatelets, Nano Lett. 15 (2015) 6521–6527.
[13] S. Parveen, K.K. Paul, R. Das, P.K. Giri, Large exciton binding energy, high photoluminescence quantum yield and improved photostability of organo-metal halide hybrid perovskite quantum dots grown on a mesoporous titanium dioxide template, J. Colloid Interface Sci. 539 (2019) 619–633.
[14] J. Ghosh, L.P.L. Mawlong, B.M. G, A.J. Pattison, W. Theis, S. Chakraborty, P. K. Giri, Solid-state synthesis of stable and color tunable cesium lead halide perovskite nanocrystals and the mechanism of high-performance photodetection in a monolayer MoS2/CsPbBr3 vertical heterojunction, J. Mater. Chem. C 8 (2020) 8917–8934.
[15] J. Ghosh, M. Hossain, P.K. Giri, Origin and tunability of dual color emission in highly stable Mn doped CsPbCl3 nanocrystals grown by a solid-state process, J. Colloid Interface Sci. 564 (2020) 357–370.
[16] G. Longo, A. Pertegas, L. Martinez-Sarti, M. Sessolo, H.J. Bolink, Highly luminescent perovskite-aluminum oxide composites, J. Mater. Chem. C 3 (2015) 11286–11289.
[17] V. Malgras, J. Henzie, T. Takei, Y. Yamauchi, Hybrid methylammonium lead halide perovskite nanocrystals confined in gyroidal silica templates, Chem. Commun. 53 (2017) 2359–2362.
[18] V. Malgras, J. Henzie, T. Takei, Y. Yamauchi, Stable blue luminescent CsPbBr3 perovskite nanocrystals confined in mesoporous thin films, Angew. Chem. 57 (2018) 8881–8885.
[19] M. Anaya, A. Rubino, T.C. Rojas, J.F. Galisteo-López, M.E. Calvo, H. Míguez, Strong quantum confinement and fast photoemission activation in CH3NH3PbI3 perovskite nanocrystals grown within periodically mesostructured films, Adv. Opt. Mater. 5 (2017), 1601087.
[20] S. Demchyshyn, J. Roemer, H. Groiß, H. Heilbrunner, C. Ulbricht, D. Apaydin, A. Böhm, U. Rütt, F. Bertram, G. Hesser, M.C. Scharber, N.S. Sariciftci, B. Nickel, S. Bauer, E.D. Głowacki, M. Kaltenbrunner, Confining metal-halide perovskites in nanoporous thin films, Sci. Adv. 3 (2017), e1700738.
[21] D. Vila-Liarte, M.W. Feil, A. Manzi, J.L. Garcia-Pomar, H. Huang, M. Döblinger, L. M. Liz-Marzán, J. Feldmann, L. Polavarapu, A. Mihi, Templated-assembly of CsPbBr3 perovskite nanocrystals into 2D photonic supercrystals with amplified spontaneous emission, Angew. Chem. Int. Ed. 59 (2020) 17750–17756.
[22] B. Wang, C. Zhang, W. Zheng, Q. Zhang, Z. Bao, L. Kong, L. Li, Large-scale synthesis of highly luminescent perovskite nanocrystals by template-assisted solid-state reaction at 800 °C, Chem. Mater. 32 (2020) 308–314.
[23] H.-C. Wang, S.-Y. Lin, A.-C. Tang, B.P. Singh, H.-C. Tong, C.-Y. Chen, Y.-C. Lee, T.-L. Tsai, R.-S. Liu, Mesoporous silica particles integrated with all-inorganic CsPbBr3 perovskite quantum-dot nanocomposites (MP-PQDs) with high stability and wide color gamut used for backlight display, Angew. Chem. Int. Ed. 55 (2016) 7924–7929.
[24] D.N. Dirin, L. Protesescu, D. Trummer, I.V. Kochetygov, S. Yakunin, F. Krumeich, N.P. Stadie, M.V. Kovalenko, Harnessing defect-tolerance at the nanoscale: highly luminescent lead halide perovskite nanocrystals in mesoporous silica matrixes, Nano Lett. 16 (2016) 5866–5874.
[25] D. Takhellambam, T.R. Meena, D. Jana, Room temperature synthesis of blue and green emitting CsPbBr3 perovskite nanocrystals confined in mesoporous alumina film, Chem. Commun. 55 (2019) 4785–4788.
[26] J.-Y. Sun, F.T. Rabouw, X.-F. Yang, X.-Y. Huang, X.-P. Jing, S. Ye, Q.-Y. Zhang, Facile two-step synthesis of all-inorganic perovskite CsPbX3 (X = Cl, Br, and I) zeolite-Y composite phosphors for potential backlight display application, Adv. Funct. Mater. 27 (2017), 1704371.
[27] S. Ye, J.-Y. Sun, Y.-H. Han, Y.-Y. Zhou, Q.-Y. Zhang, Confining Mn2+-doped lead halide perovskite in zeolite-Y as ultrastable orange-red phosphor composites for white light-emitting diodes, ACS Appl. Mater. Interfaces 10 (2018) 24656–24664.
[28] C. Zhang, B. Wang, W. Li, S. Huang, L. Kong, Z. Li, L. Li, Conversion of invisible metal-organic frameworks to luminescent perovskite nanocrystals for confidential information encryption and decryption, Nat. Commun. 8 (2017) 1138.
[29] Z. Chen, Z.-G. Gu, W.-Q. Fu, F. Wang, J. Zhang, A confined fabrication of perovskite quantum dots in oriented MOF thin film, ACS Appl. Mater. Interfaces 8 (2016) 28737–28742.
[30] J. Ghosh, R. Ghosh, P.K. Giri, Mesoporous Si nanowire templated controlled fabrication of organometal halide perovskite nanoparticles with high photoluminescence quantum yield for light-emitting applications, ACS Appl. Nano Mater. 1 (2018) 1551–1562.
[31] J. Ghosh, R. Ghosh, P.K. Giri, Strong cathodoluminescence and fast photoresponse from embedded CH3NH3PbBr3 nanoparticles exhibiting high ambient stability, ACS Appl. Mater. Interfaces 11 (2019) 14917–14931.
[32] D. Lin, Z. Wu, S. Li, W. Zhao, C. Ma, J. Wang, Z. Jiang, Z. Zhong, Y. Zheng, X. Yang, Large-area Au-Nanoparticle-Functionalized Si nanorod arrays for spatially uniform surface-enhanced Raman spectroscopy, ACS Nano 11 (2017) 1478–1487.
[33] T. Kim, X. Fu, D. Warther, M.J. Sailor, Size-controlled Pd nanoparticle catalysts prepared by galvanic displacement into a porous Si-iron oxide nanoparticle host, ACS Nano 11 (2017) 2773–2784.
[34] N. Khinevich, H. Bandarenka, S. Zavatski, K. Girel, A. Tamulevičienė, T. Tamulevičius, S. Tamulevičius, Porous silicon - a versatile platform for mass-production of ultrasensitive SERS-active substrates, Microporous Mesoporous Mater. 323 (2021), 111204.
[35] W. Li, Z. Liu, F. Fontana, Y. Ding, D. Liu, J.T. Hirvonen, H.A. Santos, Tailoring porous silicon for biomedical applications: from drug delivery to cancer immunotherapy, Adv. Mater. 30 (2018), 1703740.
[36] R. Ghosh, M.S. Song, J. Park, Y. Tchoe, P. Guha, W. Lee, Y. Lim, B. Kim, S.-W. Kim, M. Kim, G.-C. Yi, Fabrication of piezoresistive Si nanorod-based pressure sensor arrays: a promising candidate for portable breath monitoring devices, Nano Energy 80 (2021), 105537.
[37] R. Ghosh, P.K. Giri, Silicon nanowire heterostructures for advanced energy and environmental applications: a review, Nanotechnology 28 (2017), 012001.
[38] J.B. Park, M.S. Song, R. Ghosh, R.K. Saroj, Y. Hwang, Y. Tchoe, H. Oh, H. Baek, Y. Lim, B. Kim, S.-W. Kim, G.-C. Yi, Highly sensitive and flexible pressure sensors using position- and dimension-controlled ZnO nanotube arrays grown on graphene films, NPG Asia Mater. 13 (2021) 57.

[39] J. Park, R. Ghosh, M.S. Song, Y. Hwang, Y. Tchoe, R.K. Saroj, A. Ali, P. Guha, B. Kim, S.-W. Kim, M. Kim, G.-C. Yi, Individually addressable and flexible pressure sensor matrixes with ZnO nanotube arrays on graphene, NPG Asia Mater. 14 (2022) 40.
[40] H. Oh, J. Park, W. Choi, H. Kim, Y. Tchoe, A. Agrawal, G.-C. Yi, Vertical ZnO nanotube transistor on a graphene film for flexible inorganic electronics, Small 14 (2018), 1800240.
[41] H.T. Ng, J. Han, T. Yamada, P. Nguyen, Y.P. Chen, M. Meyyappan, Single crystal nanowire vertical surround-gate field-effect transistor, Nano Lett. 4 (2004) 1247–1252.
[42] Y.J. Hong, R.K. Saroj, W.I. Park, G.-C. Yi, One-dimensional semiconductor nanostructures grown on two-dimensional nanomaterials for flexible device applications, Apl. Mater. 9 (2021), 060907.
[43] Z. Huang, N. Geyer, P. Werner, J. de Boor, U. Gösele, Metal-assisted chemical etching of silicon: a review, Adv. Mater. 23 (2011) 285–308.
[44] R. Ghosh, P.K. Giri, I. Kenji, F. Minoru, Origin of visible and near-infrared photoluminescence from chemically etched Si nanowires decorated with arbitrarily shaped Si nanocrystals, Nanotechnology 25 (2014), 045703.
[45] W.-K. To, C.-H. Tsang, H.-H. Li, Z. Huang, Fabrication of n-type mesoporous silicon nanowires by one-step etching, Nano Lett. 11 (2011) 5252–5258.
[46] Y. Qu, H. Zhou, X. Duan, Porous silicon nanowires, Nanoscale 3 (2011) 4060–4068.
[47] F. Zhang, H. Zhong, C. Chen, X-g Wu, X. Hu, H. Huang, J. Han, B. Zou, Y. Dong, Brightly luminescent and color-tunable colloidal CH3NH3PbX3 (X = Br, I, Cl) quantum dots: potential alternatives for display technology, ACS Nano 9 (2015) 4533–4542.
[48] D. Aldakov, P. Reiss, Safer-by-Design fluorescent nanocrystals: metal halide perovskites vs semiconductor quantum dots, J. Phys. Chem. C 123 (2019) 12527–12541.
[49] D. Di, K.P. Musselman, G. Li, A. Sadhanala, Y. Ievskaya, Q. Song, Z.-K. Tan, M. L. Lai, J.L. MacManus-Driscoll, N.C. Greenham, R.H. Friend, Size-dependent photon emission from organometal halide perovskite nanocrystals embedded in an organic matrix, J. Phys. Chem. Lett. 6 (2015) 446–450.
[50] R. Ghosh, A. Pal, P.K. Giri, Quantitative analysis of the phonon confinement effect in arbitrarily shaped Si nanocrystals decorated on Si nanowires and its correlation with the photoluminescence spectrum, J. Raman Spectrosc. 46 (2015) 624–631.
[51] R. Ghosh, R. Das, P.K. Giri, Label-free glucose detection over a wide dynamic range by mesoporous Si nanowires based on anomalous photoluminescence enhancement, Sensor. Actuator. B Chem. 260 (2018) 693–704.
[52] M. Saliba, W. Zhang, V.M. Burlakov, S.D. Stranks, Y. Sun, J.M. Ball, M.B. Johnston, A. Goriely, U. Wiesner, H.J. Snaith, Plasmonic-induced photon recycling in metal halide perovskite solar cells, Adv. Funct. Mater. 25 (2015) 5038–5046.
[53] S. Adjokatse, H.-H. Fang, M.A. Loi, Broadly tunable metal halide perovskites for solid-state light-emission applications, Mater. Today 20 (2017) 413–424.
[54] A. Shinde, R. Gahlaut, S. Mahamuni, Low-temperature photoluminescence studies of CsPbBr3 quantum dots, J. Phys. Chem. C 121 (2017) 14872–14878.
[55] H.C. Woo, J.W. Choi, J. Shin, S.-H. Chin, M.H. Ann, C.-L. Lee, Temperature-dependent photoluminescence of CH3NH3PbBr3 perovskite quantum dots and bulk counterparts, J. Phys. Chem. Lett. 9 (2018) 4066–4074.
[56] C. Chen, X. Hu, W. Lu, S. Chang, L. Shi, L. Li, H. Zhong, J.-B. Han, Elucidating the phase transitions and temperature-dependent photoluminescence of MAPbBr3 single crystal, J. Phys. Appl. Phys. 51 (2018), 045105.
[57] D.A. Wheeler, J.Z. Zhang, Exciton dynamics in semiconductor nanocrystals, Adv. Mater. 25 (2013) 2878–2896.
[58] S. Wu, L. Cheng, Q. Wang, Excitonic effects and related properties in semiconductor nanostructures: roles of size and dimensionality, Mater. Res. Express 4 (2017), 085017.
[59] K. Zheng, Q. Zhu, M. Abdellah, M.E. Messing, W. Zhang, A. Generalov, Y. Niu, L. Ribaud, S.E. Canton, T. Pullerits, Exciton binding energy and the nature of emissive states in organometal halide perovskites, J. Phys. Chem. Lett. 6 (2015) 2969–2975.
[60] T. Ahmed, S. Seth, A. Samanta, Boosting the photoluminescence of CsPbX3 (X = Cl, Br, I) perovskite nanocrystals covering a wide wavelength range by postsynthetic treatment with tetrafluoroborate salts, Chem. Mater. 30 (2018) 3633–3637.
[61] V.G.V. Dutt, S. Akhil, R. Singh, M. Palabathuni, N. Mishra, Year-long stability and near-unity photoluminescence quantum yield of CsPbBr3 perovskite nanocrystals by benzoic acid post-treatment, J. Phys. Chem. C 126 (2022) 9502–9508.